From Reticular Chemistry Design to Density Functional Theory Modeling for New Zeolitic Imidazolate Framework Topologies: Mechanical Stability, Electronic Structure, and CO2 Selectivity

Hieu T. Hoang,[†] Ha L. Nguyen,*,[†,‡] Thang B. Phan,[†] Sareeya Bureekaew,[§] Yoshiyuki Kawazoe,[∥] Duc Nguyen-Manh,[⊥] and Hung M. Le*,[†]

[†]Center for Innovative Materials and Architectures (INOMAR), Vietnam National University, Ho Chi Minh City 721337, Vietnam
[‡]Center for Research Excellence in Nanotechnology (CENT), King Fahd University of Petroleum and Minerals, Dhahran 31261, Saudi Arabia
[§]Department of Chemical and Biomolecular Engineering, School of Energy Science and Engineering, Vidyasirimedhi Institute of Science and Technology, Rayong 21210, Thailand
[∥]New Industry Creation Hatchery Center, Tohoku University, Sendai 980-8579, Japan
[⊥]Culham Centre for Fusion Energy, United Kingdom Atomic Energy Authority, Culham Science Centre, Abingdon OX14 3DB, United Kingdom

S *Supporting Information*

ABSTRACT: Adopting the knowledge and resource of reticular chemistry, we introduce a series of new zeolitic imidazolate framework (ZIF) structures within three topological categories, **pth**, **pts**, and **ast**, constructed by the square-planar and tetrahedral building blocks. Systematic metalation is considered with various cations (i.e., Ni^{2+}, Cu^{2+}, Mn^{2+}, Co^{2+}, Zn^{2+}). Utilizing the advantage of density functional theory (DFT) calculations, we observe that the imidazole linking units suffer severe deformation in the **ast** and **pts** networks, as pointed out by the negative phonon modes. The mechanical stability is then verified by analyzing the elastic tensors (C_{ij}), and we conclude four structures to acquire mechanical stability: pth-1 (NiMn), pth-2 (NiCo), pth-3 (NiZn), and pth-6 (CuZn). Electronic structure analysis suggests the first two structures to exhibit strong magnetism, whereas the latter are weakly or even nonpolarized, which establishes good agreement with the ligand-field theory prediction. The band gaps of those structures fall in the range of 0.74 to 1.78 eV, as estimated by conventional DFT calculations. Finally, we investigate the CO_2 selectivity over N_2 within pth-1 and pth-3 by conducting grand canonical Monte Carlo simulations for gas adsorption. For the pth-1 (NiMn) and pth-3 (NiZn) cases, the load of CO_2 dominantly exceeds the uptake of N_2 at the pressure up to 1 bar, indicating those structure to be promising in CO_2 capture and selectivity.
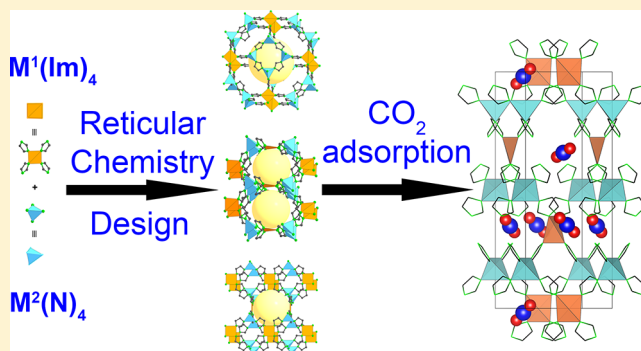
I. INTRODUCTIONS

Zeolitic imidazolate frameworks (ZIFs) are a subclass of metal−organic frameworks (MOFs), hybrid materials composed of inorganic metal secondary building units (SBUs), and organic linkers based on the carboxylate links. They are fundamentally composed of the tetrahedral building units of Zn^{2+}, Cu^{2+}, or Co^{2+} and imidazole-based linkers.[1] Not only are ZIFs regarded as a highly porous materials whose organic and inorganic nodes can be designed, modified, and functionalized to form targeted structures for certain applications, but also they have been found to be more chemically and thermally stable than MOFs because of covalent bonding owing to the linkage of tetrahedral metal ions and heteroatom (N)-based imidazole ring in the 3D network.[2] Gas storage and selective separation of CO_2 from a mixture of gas (biogas, flue gas

stream) is an emerging application[3] exploiting the capabilities of ZIFs such as high porosity, strong affinity of framework with adsorbent, and, the most pivotal factor, the suitable pore size and shape affording gas molecules to tightly interact with adsorbate. In addition, when considering the gas separation under high humidity and regeneration process, ZIFs can be reckoned as a potential candidate compared with MOFs, zeolites, and activated carbon due to their high stability under harsh working conditions (boiling water, acidic medium, high temperature) as well as low energy for the recyclability (the regeneration process requires no heating power).[4]

It should be noted that designing new ZIFs for CO_2 capture and separation still remains a challenging task because of the limit of organic linkers used in the synthesis, in which imidazole derivatives are set to react with bivalent metal sites.[4] To overcome this circumstance, the geometrical structure of linking units needs to be varied or modified to produce various kinds of points of extension.[5] This point is directly related to the phenomenon of conceptual reticular chemistry.

Reticular chemistry has evolved during the last few decades and has become an exceptionally intellectual methodology for materials science research, especially in the field of porous structures, that is, MOFs, ZIFs, and covalent organic frameworks (COFs).[6] In this context, we utilize the knowledge of reticular chemistry to derive three different kinds of ZIF topology, which include **ast**, **pth**, and **pts**. Those topologies are discussed for the first time in the ZIF chemistry, when we use four-coordination point of extension (4-**c**) generated from the $Cu(Im)_4^{2+}$ square-planar complex[7] (Scheme 1) to react with 4-

Scheme 1. Synthetic Procedure of Square-Planar Complex of $Cu(Im)_4^{2+}$ Acting as the SBU Reactant for New ZIF Construction
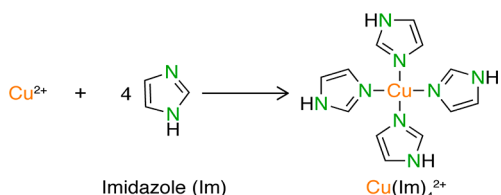
c of Zn^{2+} tetrahedral SBUs. The postsynthetic metalation (PSM) is used to exchange the Cu open sites with Ni, which is due to the challenge of Ni-imidazolate-based square-planar complex, and Zn sites with Co or Mn to form 18 new ZIF structures in total. It is noted that PSM is applied to lead experimental research in the near future to produce the multivariate metal-based ZIFs. The main purpose of this study is to employ quantum-mechanical computational modeling techniques to classify the most realistic structures among those 18 ZIFs. Subsequently, the properties of designed materials based on multivariate metal clusters are to be systematically investigated with the following highlighted aspects: geometrical and mechanical stability and full understanding of the electronic configuration by first-principles modeling, leading to our obtaining four stable structures of the **pth** network, which eventually are found to be selective for CO_2 uptake.

II. STRUCTURE DESIGN AND COMPUTATIONAL METHOD

II.1. Structural Design. It should be noted that the modification of the linking units plays a crucial role in the design and synthesis of new topological structure in the ZIF chemistry. Indeed, ZIFs mimic the nature of zeolite-type topology. To our knowledge, there are around 20 topologies found for ZIF structures compared with almost 200 networks of zeolites.[3,4] Mixed linker systems, or abundantly bulk functionalities of imidazole-based linkers, were successfully introduced to achieve new kinds of structures in ZIFs.[3−5] To get a full picture of using the modified linking units for ZIF construction, we use the precursor linker that contains four coordinations, which is the square-planar complex of Cu-$(Im)_4^{2+}$. Such a linking unit was reportedly utilized to form two

kinds of new ZIF topology, which are **ntn** and **thl**.[4] By adopting the principle of topological deconstruction governed by the Reticular Chemistry Structure Resources (RCSR) database, when connecting one kind of edge and two kinds of vertices whose coordination numbers are 4, we can find 15 possibilities of topology (see Table 1). We then consider the

Table 1. Collecting of the Statistic Information for the Topological Formation[11]

topology	vertices	edges	geometrical node
css	2	1	tetrahedron + tetrahedron
dia-b	2	1	tetrahedron + tetrahedron
icd	2	1	tetrahedron + tetrahedron
ics-b	2	1	tetrahedron + tetrahedron
lvt-b	2	1	square + square
nbo-b	2	1	square + square
pth	2	1	tetrahedron + square
pts	2	1	tetrahedron + square
ast	2	1	tetrahedron + square
btz-b	2	1	tetrahedron + tetrahedron
rhr-b	2	1	square + square
sod-b	2	1	tetrahedron + tetrahedron
ssa	2	1	square + square
ssb	2	1	square + square
ssc	2	1	square + square

geometry of the precursor, square-planar $Cu(Im)_4^{2+}$, and the tetrahedral SBUs of Zn^{2+}, leading to our finally getting the well-known **pth** and **pts** topologies that are constructed by the combination of square and tetrahedral nodes with the 1:1 ratio. We also change the ratio of square/tetrahedral SBUs to 1:2 to build up the **ast** network (Figure 1).

With the information on those topologies in hand, we further model the crystal structures of ZIF-ast, ZIF-pth, and
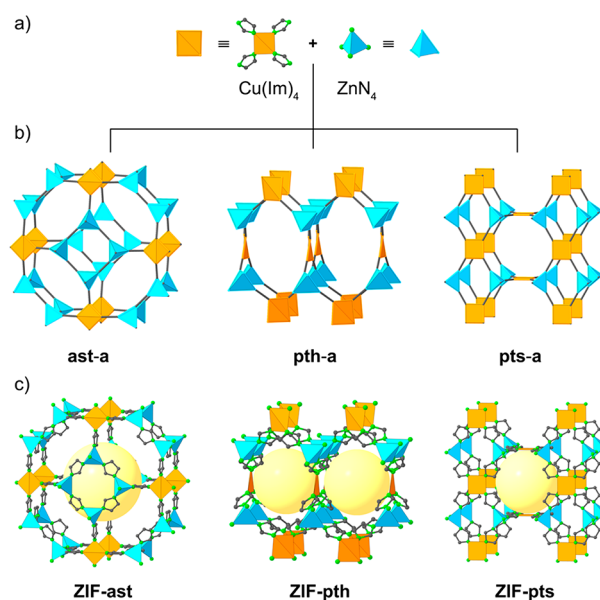

Figure 1. (a) Strategy of topological deconstruction: The combination of mixed SBUs, square-planar $Cu(Im)_4^{2-}$, and tetrahedral ZnN_4 to form three possibilities of new ZIF networks. (b) Augmented topological structures of **ast**, **pth**, and **pts**. (c) Crystal structures of corresponding ZIFs are presented to show various kinds of pores.

ZIF-pts on the basis of mixed metal cations (Table 2). After evaluating the possible nets including **pts**, **pth**, and **ast**, the

**Table 2. Crystallographic Data of Initially Constructed ZIF-ast, ZIF-pth, and ZIF-pts**

topology	lattice	space group	unit-cell parameter (Å)	pore size (Å)
ast	tetragonal	$I4/mmm$	$a = b = 19.19$; $c = 19.02$	12.0
pth	hexagonal	$P6_{2}22$	$a = b = 9.25$; $c = 21.74$	7.5
pts	tetragonal	$P4_{2}/mmc$	$a = b = 10.08$; $c = 13.80$	11.5

simplified network, which contains the node of vertices and edges based on the RCSR database, was constructed with Materials Studio.[8] The square-planar complex of Cu-imidazolate ($Cu(Im)_4^{2+}$) was built in the GaussView graphical interface,[9] which can identify the suitable resonance geometries. The plausible nets were initially comprised by connecting Cu-imidazolate, acting as a 4-**c** point of extension to the Zn^{2+} SBUs (points of extension or vertices). Those structures are subsequently optimized using the geometrical optimization functionality with the Universal Force Field (UFF)[10] in the Materials Studio software. The ZIF-pts structure crystallized in the tetragonal lattice system with the maximum space group of the **pts** topology is found to be $P4_2/mmc$, leading to constraint of the geometrical vibration of $Cu(Im)_4^{2+}$ linking parts in a planar plane. The linking of Cu^{2+} square SBUs to Zn^{2+} tetrahedral SBUs provides a square channel whose pore size is ~11.5 Å (shown in Figure 1c). In the case of **pth** topology, the hexagonal lattice is found with the space group of $P6_222$, which does not affect the constraint of the imidazole links. Thus the imidazole linking units are twisted by a certain angle to form stable geometry, resulting in the distortion of square-planar units linked to the tetrahedral building block of Zn^{2+} generating four- and eight-membered rings (Figure 1), in which the channels through four rings possess a square window of 7 Å and the pore constructed by the combination of both of four- and eight-membered rings is found to possess a 7.5 Å diameter. The largest diameter of the cage attributed to the ZIF-ast structure is 12 Å, covered by 6 of the four-membered rings and 12 of the six-membered rings (Figure 1).

Considering the similarity in binding coordination of metal cations, we explore the possibility of replacing the first metal cation site (Cu^{2+}) of the square-planar SBUs by Ni^{2+} and the tetrahedral SBUs of the second metal cation site (Zn^{2+}) by Co^{2+} or Mn^{2+}. Therefore, for the first cation site (denoted as M^1), we consider Ni^{2+} or Cu^{2+}, whereas the second cation sites (M^2) can be constituted by Mn^{2+}, Co^{2+}, or Zn^{2+}. In total, 18 new ZIF structures are proposed within three different topologies, and their structure and mechanical stability is to be verified using the first-principles calculation method. For convenience, we assign a systematic nomenclature to those 18 structures by combining the name of topology (**ast**, **pth**, and **pts**) and an integer number, as presented in Scheme 2.

There are 170 atoms in the Niggli reduced unit cell of an **ast** structure, which consists of 2 M^1, 8 M^2, and 20 Im anions. In a particular ZIF structure, the M−Im−M angle is generally observed to resemble the Si−O−Si angle in zeolites (145°). According to our optimization using an empirical force field, the M−Im−M angles are found to be 143.2°. For the **pth** topology, there are 3 M^1 and 3 M^2 in a primary unit cell containing 102 atoms; in this case, the M−Im−M angles differ

Scheme 2. Assigned Nomenclature for the 18 Proposed ZIF Structures[a]
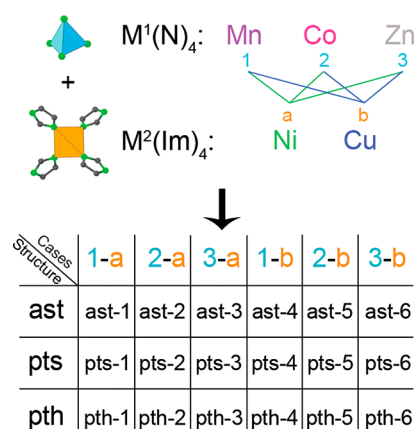
[a]For convenience, we use the name of topology and a number to indicate the network type with each (M^1, M^2) identity.

and are found to spread in a wide range from 110 to 160°. For those structures with the **pts** topology, there are 2 M^1 and 2 M^2 in a primary unit cell containing 68 atoms, with the M−Im−M angles initially optimized in the range of (95°; 155°). In the next stage, we carry out first-principles calculations to examine the structural and mechanical stability of the so-designed ZIFs.

II.2. Computational Detail for Electronic Structure Calculations. First-principles density functional theory[12,13] (DFT) calculations for the periodic ZIF structures are performed using the Vienna Ab Initio Simulation Package (VASP).[14−17] The Perdew−Burke−Ernzerhof (PBE) exchange-correlation functional[18−20] is employed with the involvement of the projector-augmented wave (PAW) method[21,22] in constructing electronic wave functions. For relatively large periodic systems, we choose the standard cutoff energy of 400 eV, which is sufficient for plane-wave expansion of the participant atoms. Upon the consideration of hexagonal unit-cell vectors, we choose the k-point mesh of (5 × 5 × 2) for the **pth** unit cells. For the **pts** and **ast** structures, we choose the k-point meshes of (5 × 5 × 4) and (3 × 3 × 3), respectively. Self-consistency is set to achieve an energy criterion of 10^{-5} eV, which is good enough for large systems with more than 100 atoms. Spin-polarization is activated to validate the spin states of metal cation sites. In each structural optimization, the unit cell and atoms are simultaneously relaxed by adopting the conjugate-gradient algorithm with an energy convergence criterion of 10^{-2} eV/Å. For the treatment of long-range van der Waals interactions, we use the semiempirical Grimme correction[23] (D3) in our calculations.

III. QUALIFICATION TESTS FOR NEW ZIF STRUCTURES

III.1. Structural Optimizations. Various optimizations with different magnetic initializations are performed to figure out all of the possibilities of different spin states and make judgment of the energetic favorability based on total energy intuition. For each compound, at least three different calculation trials are executed, in which we consider the alignment of ferromagnetic (M^1 and M^2 having similar spin alignment), nonmagnetic, and ferrimagnetic (M^1 and M^2 having partially opposite spin alignment).

III.1.1. pth Topology. We first examine the initially built structure given by empirical optimization. For the case of CuZn (pth-6), only one spin state is found with a total magnetic moment of 3 μ_B/cell. By analyzing the partial magnetic contribution, we find that the three Zn^{2+} cations do not prefer to exhibit spin polarization. In other words, the 3d orbitals of Zn do not possess unpaired electrons. Cu, on the contrary, is found to contribute a dominant magnetic moment of 0.55 μ_B, whereas Im^- also exhibits a small positive magnetic contribution.

For the case of CuMn (pth-4), two magnetic states are examined: (Cu, Mn) to have analogous spin direction (ferromagnetic, FM) and opposite spin direction (antiferromagnetic, AFM). Adopting the same magnetic behavior as seen in pth-6, Cu would prefer to establish one unpaired electron. In general, Mn^{2+} is a strongly polarized cation. In particular, we observe that in this case when M^{2+} is surrounded by four Im^- anions, each Mn^{2+} preferably establishes a very strong magnetic moment of 4.2 μ_B. More interestingly, Cu^{2+} and Mn^{2+} are found to align with opposite spin directions. In total, a magnetic moment of 12 μ_B is found. For the last **pth** candidate involving Cu^{2+} as the M^1 site (pth-5), a total magnetic moment of 6 μ_B is found, in which we again conceive a contradicting magnetic alignment of Cu^{2+} and Co^{2+}. It is not surprising that each of the Cu^{2+} cations contributes a small resisting moment of 0.5 μ_B, whereas each Co^{2+} cation exhibits 2.4 μ_B. Overall, as we attempt to optimize various magnetic states of each **pth** structure involving Cu^{2+}, all variations arrive at a particular spin alignment, in which Cu^{2+} contributes a small magnetic moment of 0.5 μ_B and has a tendency to resist the magnetic alignment of the M^2 sites (if it does exist).

Subsequently, we move on to the Ni^{2+} **pth** derivatives (pth-1, pth-2, pth-3). Within the **pth** category, pth-1 (involving Ni^{2+} and Mn^{2+}) is the only structure that exhibits two different magnetic behaviors. When considering magnetic moments with similar direction for both metal cations (FM), we obtain a magnetism of 15 μ_B. In this case, Mn^{2+} is reported to have four unpaired electrons (4.3 μ_B/metal site), whereas Ni^{2+} contributes a less significant amount. For the AFM states, Mn^{2+} again exhibits four unpaired electrons, whereas each Ni^{2+} cation gives a resisting moment of −1.4 μ_B. Actually, the total energy difference of 1.28 eV clearly indicates the favorability of the FM state. The pth-2 structure with the participation of Ni^{2+} and Co^{2+} has only one magnetic state of 9 μ_B, in which each Co^{2+} cation contributes 2.4 μ_B. The pth-3 structure does not exhibit a magnetic moment due to almost fully occupied 3d subshells. In fact, this structure is the only nonmagnetic ZIF in the **pth** topology.

III.1.2. pts Topology. The first structure pts-1 exhibits two magnetic states, 10 μ_B (high spin) and 4.59 μ_B (low spin), with the high-spin structure being more energetically stable by only 0.02 eV/unit cell, which indicates the tendency to switch between the two spin states. In the high-spin state, Ni^{2+} and Mn^{2+} align ferromagnetically with magnetic moments of 1.2 μ_B and 3.3 μ_B, respectively. In the low-spin state (AFM), the magnetic moments of the two metal cation sites are very similar in magnitude compared with those given in the FM state, but their directions are opposite. A similar behavior is seen in pts-2, where the energy gap between FM (4 μ_B/cell) and AFM (3.72 μ_B) states is 0.03 eV. In this particular case, pts-2 prefers to align antiferromagnetically, in which a Ni^{2+} site contributes 1.36 μ_B and a Co^{2+} site contributes −2.58 μ_B. For pts-3, we observe only one magnetic state (3.95/cell).

Compared with the previous nonmagnetic pts-3 structure, it is seen in this case that by adopting a different topology the electronic configurations of Ni^{2+} and Zn^{2+} yield different numbers of unpaired electrons.

The pts-4 and pts-6 structures have no more than one stable ground state. For pts-4, a magnetic moment of 7.20 μ_B/cell is observed, whereas pts-6 exhibits a weak magnetism of 1.04 μ_B/cell. In pts-4, Mn^{2+} is strongly polarized (3.4 μ_B) and dominates the magnetic contribution, whereas Cu^{2+} gives only an insignificant resisting (negative) magnetic moment. Two spin states are observed for pts-5 with the participation of Cu^{2+} and Co^{2+}, that is, 4.00 μ_B/cell (FM, stable) and 2.54 μ_B/cell (AFM, less stable by 0.05 eV). In both cases, each Co^{2+} cation exhibits a magnetic moment of 1.3 μ_B, whereas Cu^{2+} contributes a small amount of ∼0.3 μ_B (this amount is positive in the FM state or negative in the AFM state).

III.1.3. ast Topology. In the **ast** structures, the number of M^2 sites (eight cations) is dominant and is four times the number of M^1 sites (two cations). Therefore, we find large magnetic moments of 40 μ_B/cell and 24 μ_B/cell for the case of ast-1 and ast-2, in which Ni^{2+} is almost nonpolarized. Mn^{2+} (from ast-1) and Co^{2+} (from ast-2) contribute significant magnetic moments of 4.3 μ_B and 2.4 μ_B/cell, respectively. For ast-3, no spin polarization is found, as all electrons pair up in the 3d shells of Ni^{2+} and Zn^{2+}.

With the involvement of Cu^{2+}, the resultant magnetic moments of ast-4, ast-5, and ast-6 noticeably decrease in comparison with the previous corresponding cases. Among those three cases, ast-4 exhibits the largest magnetism of 38 μ_B/cell, in which Mn^{2+} contributes 4.2 μ_B and Cu^{2+} contributes an opposite magnetic moment of −0.39 μ_B. The ast-5 possesses a strong magnetic moment of 25 μ_B/cell, whereas ast-6 possesses a weak magnetic moment of 2 μ_B/cell, which mainly comes from the weak polarization of Cu^{2+}. For those particular cases, we find only one stable spin state for each of the (M^1, M^2) cationic pairs.

III.2. Stability Verification Based on Formation Energy, Phonon Vibration, and Elastic Tensor Qualification Tests.
III.2.1. Formation Energy. The first stability verification step is simply carried out by computing formation energies for all resultant ZIF structures. Let us consider a net reaction for the formation of ZIF

$$x M^1Cl_2 + y M^2Cl_2 + (2x + 2y)Im$$
$$\rightarrow ZIF + (2x + 2y)HCl \qquad (1)$$
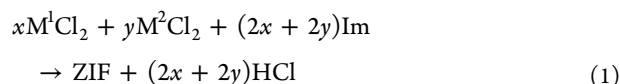
In the above net chemical reaction of imidazole with M^1Cl_2 and M^2Cl_2 (chloride salts of M^1 and M^2, respectively), a new ZIF structure and HCl are formed. Therefore, the formation energy per unit cell is calculated as

$$E_f = [E_{ZIF} + 2(x + y)E_{HCl}] - [x E_{(M^1Cl_2)} + y E_{(M^2Cl_2)}$$
$$+ 2(x + y)E_{Im}] \qquad (2)$$

where E_{ZIF}, E_{HCl}, $E_{M^1Cl_2}$, $E_{M^2Cl_2}$, and E_{Im} are the total energies of the ZIF structure, isolated HCl, M^1Cl_2, M^2Cl_2, and imidazole, respectively. A negative value of formation energy is indicative of energetic stability. All **pth** structures have negative formation energies (from −4.55 to −0.85 eV), which confirms the energetic stability of the suggested **pth** ZIF structures. For the **pts** structures, we obtain positive formation energies, an indication of thermodynamic instability (from 5.88 to 9.12 eV). For the **ast** structures, ast-2, ast-3, and ast-5 have negative

formation energies (−4.47, −0.17, and −3.15 eV, respectively), whereas the other three structures have positive formation energies (unstable).

It is obvious that each topology has a unique number of metal cations and Im⁻ anions in the unit cell; therefore, to make a comparison among structures, it is more beneficial to adopt the average stabilization energy per one imidazole molecule

$$E_{stabilize} = E_f/(2x + 2y) \qquad (3)$$

A plot of stabilization energy is presented in Figure 2 for comparison purposes. It is clearly seen that the **pts** structures
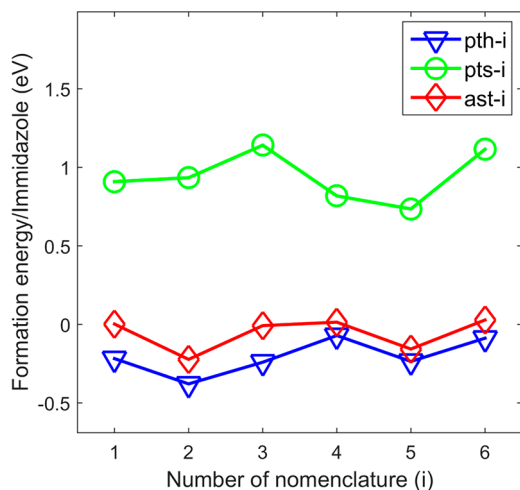

Figure 2. Stabilization energy per one imidazole molecule for the proposed ZIF structures.

are highly unstable, whereas all **pth** configurations are stable. For the **ast** network, as mentioned above, ast-2, ast-3, and ast-5 are stable. Interestingly, the **pth** topology seems to be most stable for each case of metal cation pairs. Overall, the aggregation of (M¹, M²) cations and imidazole in the **pth** network yields an amount of heat, which ensures the chemical reactions to be exothermic. We subsequently carry out two additional tests to verify the mechanical stability of each structure.

III.2.2. Phonon Analysis. As various metal cations are employed as building bridges to connect imidazole, it is obvious that different bond lengths and angles would be established because of the identity of the engaging metal. As a result, the unit cell of a particular topology involving different metals has unique cell parameters. In some cases, imidazole might be slightly or severely distorted. By saying "distorted", we refer to compressed, stretched, or bent. Unfortunately, those behaviors cannot be justified by formation energy analysis. Therefore, we carry out phonon analysis to study the vibrational modes of the designed ZIF structures and thereby re-evaluate their mechanical stability. A ZIF structure is regarded as unstable when at least one negative vibrational mode exists.

For all **pth** structures, we conceive that all vibrational wavenumbers are positive, which qualifies the six **pth** structure for the phonon test. In the phonon density of states (DOS) (Figure 3), the broad peak around 3150 cm⁻¹ is attributed to the vibration of C−H stretching. Part of the broad peak below 350 cm⁻¹ is negative due to calculation uncertainty, which reflects the translational motions in three Cartesian dimensions
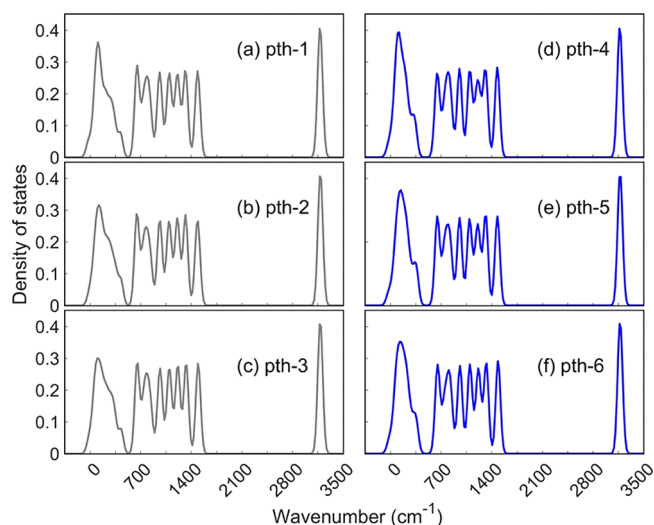

Figure 3. Phonon DOS of the six **pth** structures. All vibrational modes are positive, which proves that all metal cations and Im⁻ anions settle in a nice minimum. The small negative part of each spectrum corresponds to the three translational modes, which arises from calculation uncertainty.

of the structure. Therefore, all six **pth** structures are regarded as stable according to the second test. As we continue to observe the phonon DOS of the **pts** structures (presented in Figure 4), two negative wavenumbers are clearly found, which
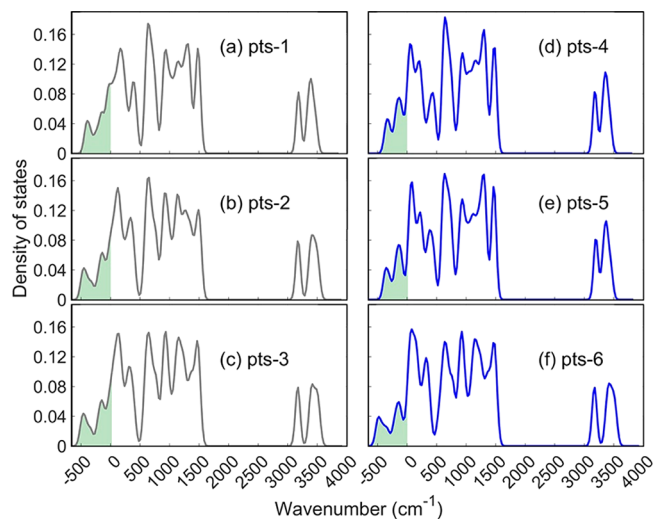

Figure 4. Phonon DOS of the six **pts** structures. Two modes around −500 and −100 cm⁻¹ are attributed to the "shaking vibration" of C−H linkages and M¹-imidazole stretch because Im⁻ suffers severe bending within the **pts** network.

are associated with the abnormal "shaking vibration" of C−H linkages and bond stretching of M¹-Im. Those imaginary vibrations are illustrated in Figure 5. Moreover, there is degeneracy on the peak above 3000 cm⁻¹ (attributed to C−H stretch) because imidazole is highly stretched to fit into the framework of **pts**. This degeneracy is not found in the previous case of **pth**. Consequently, the structures with **pts** topology are concluded to be mechanically unstable.

The negative phonon vibrational modes are also observed in the **ast** structures, as shown in Figure 6, and the **ast** structures are therefore disqualified from our mechanical stability test. In
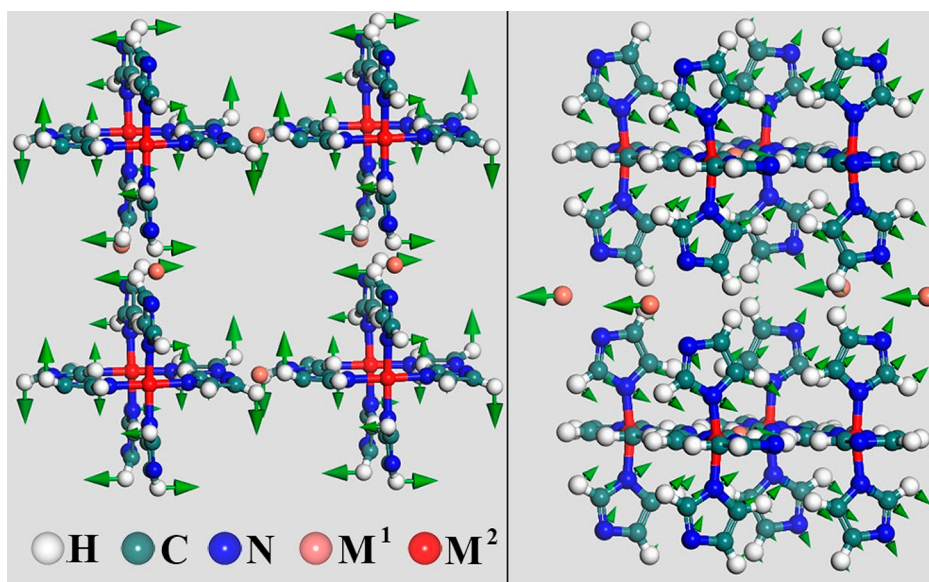
Figure 5. Illustration of the two negative modes in a particular **pts** configuration: the out-of-plane shaking vibration of C−H stretch and the M^1-Im stretching vibration.
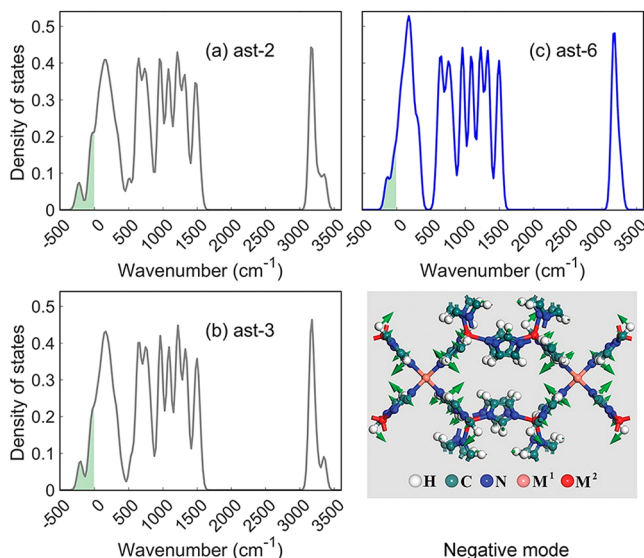

Figure 6. Three phonon DOS spectra of ast-2, ast-3, and ast-6. Two negative vibrational modes around −220 and −20 cm^{-1} associated with imidazole internal vibrations are found, which clearly indicates structural instability. The phonon spectra for the three remaining **ast** structures cannot be obtained due to failure in self-consistency as atomic positions are perturbed.

the following phonon calculations, we can only extract phonon data for ast-2, ast-3, and ast-6. For the other **ast** configurations, self-consistency in total energy calculations cannot be obtained

when ionic positions are perturbed, which accordingly reveals the instability of those structures. As shown in Figure 6, we find that two negative vibrational modes (around −220 and −20 cm^{-1}) consistently appear in the phonon DOS spectra. Unsurprisingly, the motions of those two negative modes are associated with the internal vibrations of imidazole due to suffering from severe bending within the framework.

III.2.3. Elastic Tensor Analysis. From the phonon test, all **pts** and **ast** structures are disqualified. In the final test, we perform elastic tensor calculations to examine the mechanical stability of the **pth** network. To estimate the elastic tensors using the stress−strain relationship,[24] structure perturbation with two degrees of freedom is performed. In total, six unit-cell deformations are executed on the unit-cell vectors. In addition, the contribution of ionic relaxation is also taken into account by perturbing the ionic position (six distortions for each ion in the 3D space, as previously done in the phonon calculations). With a hexagonal unit cell, each **pth** structure can be concluded to be stable if all four of the following conditions are satisfied

$$C_{11} > |C_{12}| \tag{4}$$

$$2C_{13}^2 < C_{33}(C_{11} + C_{12}) \tag{5}$$

$$C_{44} > 0 \tag{6}$$

$$C_{66} = (C_{11} - C_{12})/2 \tag{7}$$

Table 3. Calculated Elastic Modulus C_{ij} (GPa) for All pth Structures

	C_{11}	C_{12}	C_{13}	C_{33}	C_{44}	C_{66}	K	E	G
pth-1	32.2	19.1	29.6	62.9	11.1	6.5	31.5	24.7	9.0
pth-2	42.6	29.2	38.0	71.5	13.4	6.7	40.8	28.1	10.1
pth-3	39.9	26.3	34.4	65.6	11.6	6.8	37.3	25.9	9.4
pth-4	**−109.5**	**−120.3**	−86.4	−33.7	−15.8	5.4			
pth-5	**3.9**	**−10.6**	16.2	67.4	14.0	7.3			
pth-6	35.4	20.1	33.7	72.6	4.7	7.7	35.4	20.1	7.2

Condition 6 is a necessary condition to describe a hexagonal unit cell. According to our test, condition 7 is satisfied for all **pth** cases. However, because of largely negative C_{11}, pth-4 is disqualified because of the failure of inequality (eq 4). The elastic constants of pth-5 do not satisfy both inequalities (eqs 4 and 5); consequently, pth-5 is disqualified. The C_{11}, C_{12}, C_{13}, C_{33}, C_{44}, and C_{66} elastic tensors for each structure are reported in Table 3.

From the elastic tensors C_{ij}, we are able to derive three important physical quantities using the Voigt−Reuss−Hill approximation:[25] bulk (K), Young's (E), and shear (G) moduli, which depict the ability to resist compression, linear stress, and shear of a particular material. Such moduli for the four stable **pth** structures are given in Table 4. The good stability is expressed by K (31−40 GPa, equivalent to the bulk modulus of glass), which describes the capability to resist against uniform pressure.

Table 4. Adsorption Energies (eV) for CO_2 and N_2 Adsorptions in the Four Stable pth Structures

	CO_2		N_2	
	M^1	M^2	M^1	M^2
pth-1	0.51	−1.03	0.45	−0.40
pth-2	−0.27	n/a	−0.23	−1.40
pth-3	−0.01	−2.03	−0.07	−1.23
pth-6	−0.09	−2.41	−0.21	−1.49

The final test of mechanical stability by executing elasticity analysis finally eliminates pth-4 and pth-5 from our consideration. Therefore, from the initial set of 18 structures categorized in three different topologies (**pth**, **pts**, and **ast**), we conclude that pth-1 (NiMn), pth-2 (NiCo), pth-3 (NiZn), and pth-6 (CuZn) are stable according to phonon and elastic tensor analyses.

IV. ELECTRONIC STRUCTURES AND GAS ADSORPTION CAPABILITY OF THE STABLE pth STRUCTURES

IV.1. Electronic Structure. The electronic structure of each stable structure, in terms of band gap and magnetic alignment, is important, as it is relevant to the excited state and number of unpaired electrons of the metal site if a particular ZIF structure in this study is used for future reaction catalysis.[26−28] Therefore, we analyze the electronic gap between the highest occupied (HO) and lowest unoccupied (LU) states in conjunction with magnetic alignment of each stable **pth** structure by examining the partial density of states (PDOS) of M^1, M^2, and Im⁻. For pth-1, we have discussed in the previous section that the ferromagnetic state is preferred with a total magnetic moment of 15 μ_B/cell. In particular, whereas three Ni²⁺ sites contribute a fairly small magnetic sum (∼0.09 μ_B), three Mn²⁺ sites are highly polarized (4.26 μ_B for each cation). The total magnetic moment is 15 μ_B/cell. On average, the presence of each tetrahedral Mn²⁺ cation would produce a net magnetic moment of 5 μ_B. Because Im⁻ anion is an intermediate-field ligand, the splitting energy between the e_g and t_{2g} states is relatively narrow. Hence, we can hypothesize that the five electrons of Mn²⁺ (d⁵ configuration) spread out to occupy the two e_g and three t_{2g} states in an adequate manner, as illustrated in Figure 7. The DOS of occupation can be seen in Figure 8a. The α-spin of Mn²⁺ seems to contribute
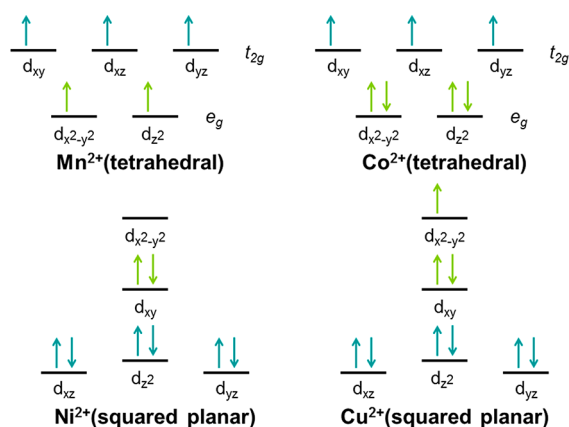

Figure 7. Occupation of 3d electrons in the degenerate orbital states of tetrahedral Mn²⁺, Co²⁺ and square-planar Ni²⁺, Cu²⁺ using ligand-field-theory interpretation.
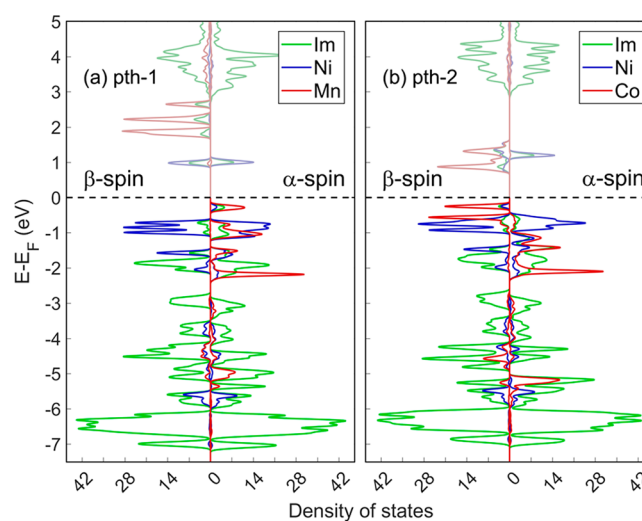

Figure 8. Electronic PDOS of pth-1 and pth-2.

significantly to constitute the HO state, whereas both α- and β-spin of Ni²⁺ take part in the formation of the HO-1 state. By examining the occupied and unoccupied eigenstates, we find that pth-1 possesses an indirect HO−LU gap of 1.21 eV. The LU state is, however, constituted by the 3d shells of Ni²⁺ and Im⁻, and the contribution of Mn²⁺ to this virtual state is very insignificant. Such PDOS occupation of electronic states helps to explain the indirect band gap behavior, as previously mentioned.

The pth-2 is another strongly polarized structure with a total magnetic moment of 9 μ_B/cell. In this structure, Ni²⁺ is observed to polarize very weakly. The total magnetic alignment of three Ni²⁺ cations is ∼0.09 μ_B, which is very similar to that found in the case of pth-1. Each Co²⁺ site contributes 2.41 μ_B, which is smaller than the magnetic alignment of Mn²⁺ in pth-1. In this case, the presence of each tetrahedral Co²⁺ cation with d⁷ electron configuration induces a net magnetic moment of 3 μ_B, which is in good agreement with our prediction based on the crystal-field theory. By examining the PDOS in Figure 8b, we observe that the HO and LU states are formed mainly with the β-spin electrons from the 3d orbitals of Co²⁺. Literally, an indirect HO−LU gap of pth-2 is observed as 0.96 eV. At this point, for the two strongly polarized structures (pth-1 and pth-2), we observe that the M^2 site actually plays an important role

in constituting the HO state. The Ni^{2+} site (d^8), however, would have two unpaired electrons if it adopts a tetrahedral bonding scheme or no unpaired electrons in the case of square-planar coordination. Actually, the optimized structures of pth-1 and pth-2 show that the square-planar coordination prevails, which is consistent with our initial design. Therefore, Ni^{2+} is nonmagnetic as a consequence.

In the two later cases (pth-3 and pth-6), the scenario in electronic structure is much different; that is, the M^2 sites do not play a decisive role in the HO−LU gap anymore. In particular, for the nonmagnetic NiZn case (pth-3), both HO and LU states are jointly constituted by Zn^{2+} and Im^-, as revealed by the PDOS in Figure 9a. The role of M^1 (i.e., Ni^{2+})
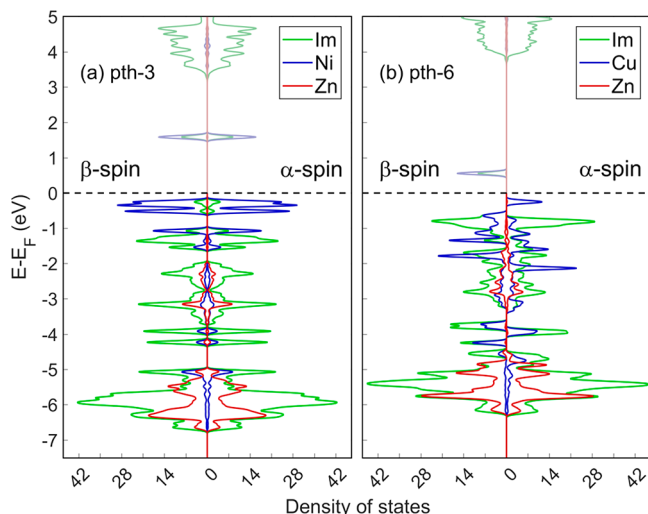

Figure 9. Electronic PDOS of pth-3 and pth-6.

in the bonding orbitals is very subtle. In fact, we observe that the orbitals of Ni^{2+} occupy low-energy states around −2 eV. Whereas Zn^{2+} (d^{10}) behaves as a nonmagnetic site, all 3d electrons of Ni^{2+} in this case also prefer to pair up, as consistently found in the previous cases of pth-1 and pth-2. As a consequence, the α- and β-electrons prefer to jointly occupy the bonding eigenstates, which leads to the overall nonspin polarization for the whole structure. Like the previous cases, an indirect HO−LU gap is observed, in this case as 1.78 eV.

The pth-6 structure possesses a small indirect band gap of 0.74 eV. Interestingly enough, this is the sole case in the entire study in which we observe the major contribution of Im^- in both HO and LU eigenstates. The 3d electron of Cu^{2+} and Zn^{2+}, on the contrary, prefers to occupy a lower energy level, as shown in Figure 9b. Each Cu^{2+} site exhibits a magnetic moment of 0.55 μ_B, whereas Zn^{2+} remains almost non-polarized. Because of its contribution to the high occupation levels, Im^- is found to be polarized as well. The net sum magnetic contribution of all Im^- anions in the whole structure is nearly 1 μ_B, which is somewhat remarkable considering the total magnetization of 3.0 μ_B/cell reported by our calculations. Overall, the presence of each tetrahedral Cu^{2+} cation induces a magnetic moment of 1 μ_B, which is in good agreement with the explanation using the crystal-field theory.

IV.2. CO_2 Selectivity. In this section, we validate the CO_2 adsorbing capability of the four stable **pth** structures. First, a gas molecule (either CO_2 or N_2) is introduced into the ZIF structure near a specific metal site (M^1 or M^2). Full structural optimizations with unit-cell relaxations are executed to search

for the most suitable adsorption site. The binding strength can be verified by analyzing the energetic favorability between CO_2 and N_2 through total energy analysis. To be specific, the binding energy of a particular case will be computed as

$$E_{binding} = E_{ZIF} + E_{gas} - E_{adsorbed-gas} \qquad (8)$$

In the equation above, E_{ZIF}, E_{gas}, and $E_{adsorbed-gas}$ are the total energies of ZIF, isolated gas molecules (CO_2 or N_2), and the complex system of a gas molecule encapsulated by ZIF. A positive value of adsorption energy is indicative of stable adsorption. In all adsorption cases, we notice that N_2 can hardly find a stable binding position to the metal sites on the framework. Initially, we place a nitrogen molecule close to either a M^1 or M^2 site. At the end of the optimization, N_2 is found to locate in the middle of a pore and establish minimal connection to the surrounding metals. In particular, the binding energies of N_2 to the M^2 site in pth-3 and pth-6 are −2.41 and −2.03 eV, respectively, which clearly indicates strong repulsion. For pth-2, we even confront a divergent optimization with N_2 adsorption, whereas the M^2 site in pth-1 is quite less repulsive to N_2 with an adsorption energy of −1.03 eV.

In general, it should be noted that the M^1 cationic site is less repulsive (in other words, more attractive) to both CO_2 and N_2 adsorptions than the M^2 site, regardless of the metal identity. It is found for pth-2, pth-3, and pth-6 that N_2 possesses adsorption energies from −0.07 to −0.23 eV. In the case of pth-1, the adsorption energy is positive (0.45 eV), which indicates that N_2 finds a good settlement in the pore.

For CO_2 adsorption, the M^2 site is more repulsive to the gas molecule than that seen in the N_2 adsorption case. The adsorption energies are found in the range of −1.03 to −2.41 eV. On the contrary, the M^1 site seems to be more promising in capturing CO_2. In particular, the M^1 sites in pth-2, pth-3, and pth-6 possess quite negative adsorption energies from −0.01 to −0.27 eV. For pth-1, we obtain a positive adsorption energy of 0.51 eV, which is stronger than the adsorption of N_2 inside pth-1. We summarize the adsorption energies of CO_2 and N_2 within the four stable **pth** structures in Table 4.

Overall, in most cases, we observe that the M^1 site is more attractive to both CO_2 and N_2. Moreover, CO_2 is shown to be more favorable inside the ZIF structures in most cases (pth-1, pth-3, pth-6), except for the case of pth-2, as we conceive that the N_2 adsorption is slightly more favorable than the CO_2 adsorption. Among the four stable **pth** structures, pth-1 seems to be very promising in the application of CO_2 capture and selectivity.

To unveil the portrait of CO_2 and N_2 uptakes, we subsequently carry out a grand canonical Monte Carlo (GCMC) simulation for the adsorption of each type of gas in the pores of pth-1 and pth-3. It should be noted that because of the different choice of cationic pairs, pth-3 exhibits a larger volume by 8% in comparison with pth-1 (321 vs 297 $Å^3$). The GCMC simulations using the μVT scheme are executed using the RASPA package,[29] which has been used extensively to investigate the gas adsorption behavior in MOFs.[30,31] In the current simulation, we employ the semiempirical force field with pairwise Lennard-Jones potentials developed for MOF applications.[32] The simulation temperature is fixed at 25 °C, whereas the pressure is varied in the range of [0; 1 bar]. For each simulation, we perform 10^6 cycles of initial equilibration and 10^6 cycles of assembling. The net atomic electrostatic charge of the framework structure is computed using the

density derived electrostatic and chemical (DDEC6) method[33−35] based on the DFT-optimized structure.

The resultant isotherm curves are presented in Figure 10. In total, four cases are presented for CO_2 and N_2 adsorptions. For
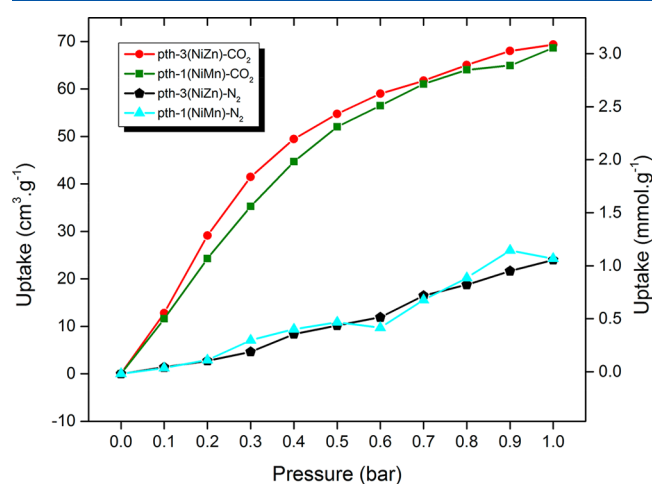

Figure 10. Isotherm curves for the CO_2 and N_2 uptakes within the pth-1 (NiMn) and pth-3 (NiZn) structures derived from GCMC calculations with μVT ensembling at 25 °C.

all N_2 cases, we observe that the uptake does not exceed 24.2 cm^3/g. The CO_2 uptake levels of pth-1 and pth-3 at the maximum investigated pressure (1 bar) completely outreach the uptake of N_2. Those uptake quantities are 68.6 and 69.3 cm^3/g, respectively. This is in good accordance from the binding energy predicted by DFT (Table 4), which predicts that the adsorption of a single CO_2 is more favorable than the adsorption of N_2. The binding energy analysis points out that pth-3 would be less attractive to gas molecule than pth-1. However, both pth-1 and pth-3 seem to possess similar gas uptake capacity. As a result, we believe that the larger volume of pth-3 is helpful in gaining the uptake amount of CO_2 in the gas capture scheme. At 1 bar, the CO_2 working capacity in each case is ∼3.1 mmol/g, which is relatively good. For comparison purposes, one may consult the level of CO_2 working capacity in the hypothetical MOFs presented by Wilmer et al.[36] Hence, we believe those two **pth** structures are good candidates for CO_2 capture and selectivity.

V. SUMMARY

In this study, adopting the power of reticular chemistry and RCSR database to combine two different kinds of SBUs including square-planar $[Cu(Im)_4]^{2+}$ complex and tetrahedral building block of Zn^{2+}, we have hypothetically developed a series of new ZIF structures within three topological categories: **pth**, **pts**, and **ast**. Those structural networks are systematically metalated to give a series of isoreticular structures with various metal SBUs (i.e., Ni^{2+}, Co^{2+}, Mn^{2+}) whose geometrical and mechanical stability are subsequently examined using first-principles DFT calculations. In addition, we carry out qualification tests to suggest the most stable candidates as a reference for future experimental syntheses. The phonon test points out that the imidazole linking units have to undergo severe deformation in the **ast** and **pts** networks. As a result, the internal vibrations of imidazole indicate that the linker is not in relaxation form; instead, it is in a saddle curvature as negative (imaginary) vibrational

frequencies are obtained, which leads to the conclusion that the **ast** and **pts** topological networks are unstable.

The third test of elastic tensors actually eliminates two other candidates, which are pth-4 and pth-5. Finally, we conclude that four structures are stable: pth-1 (NiMn), pth-2 (NiCo), pth-3 (NiZn), and pth-6 (CuZn). Electronic configuration and band structure analyses suggest that pth-1 and pth-2 are strongly polarized due to the presence of Mn^{2+} and Co^{2+}, respectively. In any case, the M^1 site (Ni^{2+} or Cu^{2+}) is weakly polarized. Moreover, the participation of Zn^{2+} at the M^2 position actually diminishes spin polarization. As for pth-3, we even conceive a nonmagnetic case, whereas pth-6 only exhibits a net magnetic moment of 3 μ_B/cell. In terms of band gap, all four stables structures are found to possess indirect gaps in the range of 0.74 to 1.78 eV. Lastly, with those validated stable structures in hand, we further investigate if the CO_2 selectivity over N_2 displays a potential performance, as we expect for CO_2-selective capture. First, the DFT binding energies suggest that pth-1 and pth-3 favor CO_2 over N_2. Then, the GCMC simulation for CO_2 and N_2 adsorptions within pth-1 and pth-3 is executed to truly understand the gas uptake process. In general, we observe that the loads of CO_2 within pth-1 and pth-3 dominantly outreach the uptake of N_2. Such observation depicts pth-1 (NiMn) and pth-3 (NiZn) as promising candidates for CO_2 capture and selectivity.

In conclusion, we believe that our designed structures and the so-found properties based on molecular modeling can be a good reference to obtain new ZIF structures, which not only possess new topology but also endure harsh working conditions (high pressure, as shown by the bulk, Young's, and shear moduli). In addition, the multivariate metalation active center in porous ZIF structures utilizing the open metal sites is designed for the first time in ZIF chemistry. Our final effort, at the end of the story, is subjected to extend further application of CO_2 capture and sequestration.

■ ASSOCIATED CONTENT

Ⓢ Supporting Information

The Supporting Information is available free of charge on the ACS Publications website at DOI: 10.1021/acs.jpcc.8b07159.

Optimized structure with the pth-1 topology (CIF)

Optimized structure with the pth-2 topology (CIF)

Optimized structure with the pth-3 topology (CIF)

Optimized structure with the pth-4 topology (CIF)

Optimized structure with the pth-5 topology (CIF)

Optimized structure with the pth-6 topology (CIF)

Optimized structure with the ast-1 topology (CIF)

Optimized structure with the ast-2 topology (CIF)

Optimized structure with the ast-3 topology (CIF)

Optimized structure with the ast-4 topology (CIF)

Optimized structure with the ast-5 topology (CIF)

Optimized structure with the ast-6 topology(CIF)

Optimized structure with the pts-1 topology (CIF)

Optimized structure with the pts-2 topology (CIF)

Optimized structure with the pts-3 topology (CIF)

Optimized structure with the pts-4 topology (CIF)

Optimized structure with the pts-5 topology (CIF)

Optimized structure with the pts-6 topology (CIF)

■ AUTHOR INFORMATION

Corresponding Authors

*E-mail: hung.m.le@hotmail.com, lmhung@inomar.edu.vn (H.M.L.)

*E-mail: nlha@inomar.edu.vn (H.L.N.).

ORCID ⊙

Ha L. Nguyen: 0000-0002-4977-925X

Sareeya Bureekaew: 0000-0001-9302-2038

Hung M. Le: 0000-0003-4060-9008

Notes

The authors declare no competing financial interest.

■ REFERENCES

(1) Banerjee, R.; Furukawa, H.; Britt, D.; Knobler, C.; O'Keeffe, M.; Yaghi, O. M. Control of Pore Size and Functionality in Isoreticular Zeolitic Imidazolate Frameworks and Their Carbon Dioxide Selective Capture Properties. *J. Am. Chem. Soc.* **2009**, *131*, 3875−3877.

(2) Huang, X.-C.; Lin, Y.-Y.; Zhang, J.- P.; Chen, X.-M. Ligand-Directed Strategy for Zeolite-Type Metal-Organic Frameworks: Zinc(II) Imidazolates with Unusual Zeolitic Topologies. *Angew. Chem., Int. Ed.* **2006**, *45*, 1557−1559.

(3) Nguyen, N. T.; Furukawa, H.; Gándara, F.; Nguyen, H. T.; Cordova, K. E.; Yaghi, O. M. Selective Capture of Carbon Dioxide under Humid Conditions by Hydrophobic Chabazite-Type Zeolitic Imidazolate Frameworks. *Angew. Chem., Int. Ed.* **2014**, *53*, 10645−10648.

(4) Nguyen, N. T.; Lo, T. N.; Kim, J.; Nguyen, H. T.; Le, T. B.; Cordova, K. E.; Furukawa, H. Achievement of Bulky Homochirality in Zeolitic Imidazolate-Related Frameworks. *Inorg. Chem.* **2016**, *55*, 6201−6207.

(5) Yang, J.; Zhang, Y. B.; Liu, Q.; Trickett, C. A.; Gutiérrez-Puebla, E.; Monge, M. A.; Cong, H.; Aldossary, A.; Deng, H.; Yaghi, O. M. Principles of Designing Extra-Large Pore Openings and Cages in Zeolitic Imidazolate Framesworks. *J. Am. Chem. Soc.* **2017**, *139*, 6448−6455.

(6) Yaghi, O. M. Reticular Chemistry − Construction, Properties, and Precision Reactions of Frameworks. *J. Am. Chem. Soc.* **2016**, *138*, 15507−15509.

(7) McFadden, D. L.; McPhail, A. T.; Gross, P. M.; Garner, C. D.; Mabbs, F. E. Crystal and Molecular Structure, Electron Spin Resonance, and Electronic Spectrum of Tetrakis(imidazole)-dinitratocopper(II). *J. Chem. Soc., Dalton Trans.* **1976**, 47−52.

(8) *Materials Studio*, version 6.0; Accelrys Software: San Diego, CA.

(9) Aeleen, F.; Hrant, P. H.; Roy, D. D., II; Todd, A. K.; John, M.; Alice, B. N.; Andrew, J. H.; Joanne, H. *GaussView*, version 5.0; Gaussian, Inc.: Wallingford, CT, 2009.

(10) Rappe, K. A.; Casewit, J. C.; Colwell, S. K.; Goddard, A. W., III; Skiff, M. W. UFF, a full periodic table force field for molecular mechanics and molecular dynamics simulations. *J. Am. Chem. Soc.* **1992**, *114*, 10024−10035.

(11) O'Keeffe, M.; Peskov, M. A.; Ramsden, S. J.; Yaghi, O. M. The Reticular Chemistry Structure Resource (RCSR) Database of, and Symbols for, Crystal Nets. *Acc. Chem. Res.* **2008**, *41*, 1782−1789.

(12) Hohenberg, P.; Kohn, W. Inhomogeneous Electron Gas. *Phys. Rev.* **1964**, *136*, B864−B871.

(13) Kohn, W.; Sham, L. J. Self-Consistent Equations Including Exchange and Correlation Effects. *Phys. Rev.* **1965**, *140*, A1133−A1138.

(14) Kresse, G.; Hafner, J. Ab Initio Molecular Dynamics of Liquid Metals. *Phys. Rev. B: Condens. Matter Mater. Phys.* **1993**, *47*, 558−561.

(15) Kresse, G.; Hafner, J. Ab Initio Molecular-Dynamics Simulation of the Liquid-Metal-Amorphous-Semiconductor Transition in Germanium. *Phys. Rev. B: Condens. Matter Mater. Phys.* **1994**, *49*, 14251−14269.

(16) Kresse, G.; Furthmüller, J. Efficient Iterative Schemes for Ab Initio Total-Energy Calculations Using a Plane-Wave Basis Set. *Phys. Rev. B: Condens. Matter Mater. Phys.* **1996**, *54*, 11169−11186.

(17) Kresse, G.; Furthmüller, J. Efficiency of Ab-initio Total Energy Calculations for Metals and Semiconductors Using a Plane-Wave Basis Set. *Comput. Mater. Sci.* **1996**, *6*, 15−50.

(18) Perdew, J. P.; Burke, K.; Ernzerhof, M. Generalized Gradient Approximation Made Simple. *Phys. Rev. Lett.* **1996**, *77*, 3865−3868.

(19) Perdew, J. P.; Burke, K.; Ernzerhof, M. Generalized Gradient Approximation Made Simple. *Phys. Rev. Lett.* **1997**, *78*, 1396−1396.

(20) Becke, A. D. Perspective: Fifty Years of Density-Functional Theory in Chemical Physics. *J. Chem. Phys.* **2014**, *140*, 18A301.

(21) Blöchl, P. E. Projector Augmented-Wave Method. *Phys. Rev. B: Condens. Matter Mater. Phys.* **1994**, *50*, 17953−17979.

(22) Kresse, G.; Joubert, D. From Ultrasoft Pseudopotentials to the Projector Augmented-Wave Method. *Phys. Rev. B: Condens. Matter Mater. Phys.* **1999**, *59*, 1758−1775.

(23) Grimme, S.; Antony, J.; Ehrlich, S.; Krieg, H. A Consistent and Accurate Ab Initio Parametrization of Density Functional Dispersion Correction (DFT-D) for the 94 Elements H-Pu. *J. Chem. Phys.* **2010**, *132*, 154104.

(24) Le Page, Y.; Saxe, P. Symmetry-General Least-Squares Extraction of Elastic Data for Strained Materials from Ab Initio Calculations of Stress. *Phys. Rev. B: Condens. Matter Mater. Phys.* **2002**, *65*, 104104.

(25) Hill, R. The elastic behaviour of a crystalline aggregate. *Proc. Phys. Soc., London, Sect. A* **1952**, *65*, 349−354.

(26) Truong, T.; Hoang, T. M.; Nguyen, C. K.; Huynh, Q. T. N.; Phan, N. T. S. Expanding applications of zeolite imidazolate frameworks in catalysis: synthesis of quinazolines using ZIF-67 as an efficient heterogeneous. *RSC Adv.* **2015**, *5*, 24769.

(27) Nguyen, V. D.; Nguyen, C. K.; Tran, K. N.; Tu, T. N.; Nguyen, T. T.; Dang, H. V.; Truong, T.; Phan, N. T. S. Zeolite imidazolate frameworks in catalysis: Synthesis of benzimidazoles via cascade redox condensation using Co-ZIF-67 as an efficient heterogeneous catalyst. *Appl. Catal., A* **2018**, *555*, 20−26.

(28) Tran, U. P. N.; Le, K. A.; Phan, N. T. S. Expanding applications of Metal-Orgamic Framworks ZIF-8 as an efficient heterogeneous catalyst for the knoeveagel reaction. *ACS Catal.* **2011**, *1*, 120−127.

(29) Dubbeldam, D.; Calero, S.; Ellis, D. E.; Snurr, R. Q. RASPA: Molecular Simulation Software for Adsorption and Diffusion in Flexible Nanoporous Materials. *Mol. Simul.* **2016**, *42*, 81−101.

(30) Xuan Huynh, N. T.; Na, V.; Chihaia, V.; Son, D. N. A Computation Approach towards Understanding Hydrogen Gas Adsorption in Co-MIL-88A. *RSC Adv.* **2017**, *7*, 39583.

(31) Becker, T. M.; Heinen, J.; Dubbeldam, D.; Lin, L.-C.; Vlugt, T. J. H. Polarizable Force Field for CO_2 and CH_4 Adsorption in M-MOF-74. *J. Phys. Chem. C* **2017**, *121*, 4659−4673.

(32) Jones, J. E. On the Determination of Molecular Fields. —II. From the Equation of State of a Gas. *Proc. R. Soc. London, Ser. A* **1924**, *106*, 463−477.

(33) Manz, T. A.; Limas, N. G. Introducing DDEC6 atomic population analysis: part 1. Charge partitioning theory and methodology. *RSC Adv.* **2016**, *6*, 47771−47801.

(34) Limas, N. G.; Manz, T. A. Introducing DDEC6 atomic population analysis: part 2. Computed results for a wide range of periodic and nonperiodic materials. *RSC Adv.* **2016**, *6*, 45727−45747.

(35) Manz, T. A. Introducing DDEC6 atomic population analysis: part 3. Comprehensive method to compute bond orders. *RSC Adv.* **2017**, *7*, 45552−45581.

(36) Wilmer, E. C.; Farha, K. O.; Bae, S. Y.; Hupp, T. J.; Snurr, Q. R. Structure-property relationships of porous materials for carbon dioxide separation and capture. *Energy Environ. Sci.* **2012**, *5*, 9849.